Polymer Journal (2018) 50:1121–1138
https://doi.org/10.1038/s41428-018-0103-1

FOCUS REVIEW

Interfacial morphologies and associated processes of multicomponent polymers

Hiroshi Jinnai[1]

Received: 10 April 2018 / Revised: 25 May 2018 / Accepted: 28 May 2018 / Published online: 13 July 2018

Abstract

This review describes contemporary advancements in the study of interfacial morphologies and associated processes of multicomponent polymers. A particular emphasis is placed on the use of three-dimensional (3D) microscopy, for example, transmission electron microtomography (TEMT) and laser scanning confocal microscopy (LSCM). The time evolution of a spinodal interface during the phase separation of a polymer blend was followed by LSCM. The obtained 3D interfacial morphology was analyzed by differential geometry. The scalability was tested using curvature distributions. 3D nanoimaging, that is, TEMT, was applied to examine the stability and dynamics of complex block copolymer (BCP) morphologies, and novel structural data were directly assessed according to the 3D volume data. This review also examines two essential developments in the time-dependent in situ electron tomography of polymer materials to study the dynamic processes of BCPs. The 3D microscopy-based structural information renders an important perspective into the studies of nonlinear nonequilibrium occurrences as well as the statistical physics of long-chain-bearing moieties.

Introduction

Polymer materials are a constant feature of contemporary life. They come in multicomponent [1–4] and block copolymer (BCP) varieties [5, 6]. Phase separation, however, often occurs in multicomponent polymer materials owing to repulsive interactions between the polymer constituents. Increasingly, more studies are being undertaken on phase-separated structures. This has been warranted partly due to the need for new industrial materials and complex fluids. The pattern formation and self-assembly of polymer blends constitute the primary focus of research into nonlinear, nonequilibrium phenomena [2, 3].

Altering a polymer blend from its single phase to the two-phase or spinodal region by changing its thermodynamic variables often causes the thermodynamically unstable mixture to separate into two phases. This occurs through spinodal decomposition (SD), during which a bicontinuous two-phase structure forms. This is usually transient and occurs in different condensed atomic and molecular systems including simple fluid mixtures, metallic alloys, and inorganic glasses [1, 7]. Several scattering studies [8–17] on SD are available. These include the time evolutions of structural properties, for example, the wavelengths of structures that have undergone phase separation. During late-phase SD, excess free energy localizes at the boundary between two phases, and the structure evolves to reduce the system interfacial energy as well as the interface area.

BCPs also phase separate into structures called "micro-phase-separated nanostructures," which form as a result of chemical junctions within the polymer molecule. BCPs cannot phase separate into micron-scale structures owing to the covalent bonds between component block chains. During phase separation, these chemical junctions must be at the interface while microdomain-forming blocks must evenly fit into the attendant microdomains. As a result, BCP morphologies are analyzed within the statistical purview of long-chain-bearing moieties.

BCP nanostructures have certain topological properties similar to those of other self-organized polymers including surfactants and lipids. As a result, the notion of a constant mean curvature (CMC) minimal surface has emerged [18] to shed some insights into the durability of complex BCP

✉ Hiroshi Jinnai
hiroshi.jinnai.d4@tohoku.ac.jp

[1] Institute of Multidisciplinary Research for Advanced Materials (IMRAM), Tohoku University, 2-1-1, Katahira, Aoba-ku, Sendai 980-8577, Japan

nanostructures. The full characterization of surface topology requires quantitative measurements of surface curvatures. Some researchers aver that the area-averaged mean curvature, $\langle H \rangle$, influences gross morphology (e.g., lamellar, bicontinuous, cylindrical, or spherical), while the standard deviation of the mean curvature distribution, σ_H, shapes the mild durability of nanostructures including gyroid (DG), double-diamond (DD), or hexagonally perforated lamellar (HPL) morphologies. This consideration follows from the notion of "packing frustration" [19]. The implication is that when the interface moves toward a CMC, the mean curvature will not be constant everywhere along the interface because the microdomain-forming blocks must fit into the space in the most entropically viable way.

Like SD in polymer blends, BCPs involve dynamic processes. A representative example of such a dynamic process is the order–order transition (OOT), which usually associates epitaxially with the morphologies of the two phases. The phase change associated with the DG morphology (in terms of to and from) has been well studied [20–23]. Such dynamic phenomena can be regarded as an interfacial rearrangement from one topology to the other and are likewise owing to the results of a subtle balance between the interface minimization and packing frustration of block chains. Consequently, interfacial morphologies and their dynamic processes play significant roles in many aspects of multicomponent polymers.

Morphological studies, including those related to interfacial morphology, of multicomponent polymeric materials are usually conducted through scattering and microscopy techniques. Transmission electron microscopes (TEMs), optical microscopes, scanning electron microscopes, and atomic force microscopes are frequently employed in investigating these phenomena. The microscope's hallmark lies in its provision of real-space relationship characterizations depending on the scattering method. Although this paper does not provide details associated with scattering methods, to fully evaluate identifiable morphologies, these data are initially attained by microscopy and then by scattering to evaluate structural indices using a morphological model obtained from the microscopy observations. This underscores how microscopy and scattering complement each other.

Yet, the complex nature of polymer (nano)structures, as increasingly revealed through progress in polymerization precision technologies [24–27], underscores the difficulty associated with identifying complex morphologies. This is largely owed to the fact that conventional microscopes only generate two-dimensional (2D) images of three-dimensional (3D) objects. Such 2D images are of no use as the (nano) structures become more and more intricate. This makes interpreting the associated scattering data difficult. Hence, only novel microscopy techniques with a 3D image-rendering capacity such as transmission electron microtomography (TEMT), X-ray computed tomography (CT) and laser scanning confocal microscopy (LSCM) are used. Thus, microscopy and scattering are complementary. Although studies using X-ray CT are not described here, the technique is very useful to observe the 3D structures of polymer systems at the micron-scale [28, 29].

This article is structured as follows: The next section engages the time evolution of the 3D bicontinuous interface of a polymer mixture undergoing phase separation during late-stage SD. LSCM was utilized to visualize the complex interface topology for the first time. In the section "Interfacial morphologies of block copolymers," complex 3D interface morphologies of various BCPs, including the DG morphology and an intriguing double-helical structure of a triblock terpolymer, are presented. The interfacial curvature distributions of a bicontinuous DG morphology were directly assessed to demonstrate that the DG interface does not show CMC and to demonstrate the relevance of packing frustration to stabilizing nanostructures. Double-helical nanostructures and complex grain morphologies from the simplest BCP morphology to the lamellar morphology are also examined in 3D. The dynamic processes in BCPs are presented in the penultimate section. The OOT between G and cylindrical morphologies has been extensively studied, and a new epitaxial pathway has been discovered. Finally, recent key developments in TEM for in situ direct imaging of BCP dynamic processes are also discussed.

Interfacial morphologies of phase-separated structures in polymer blends

Direct 3D visualization of phase-separating bicontinuous structures

This section describes real-space 3D observations associated with the bicontinuous structure of a polymer blend undergoing phase separation. It uses a binary mixture of deuterated polybutadiene (DPB) and polybutadiene (PB). Jinnai et al. [30] have provided extensive information concerning the DPB/PB mixture such as its molecular characteristics, phase diagram, and sample preparation. Thermally annealing the mixture led to a bicontinuous structure that evolved according to SD. After phase separation, LS experiments were conducted [30]. As the phase-separated structure grew, the scattering maximum shifted toward small wavenumbers reflecting the structural growth during the time range the LSCM experiments were performed in which the amplitudes of changes in concentration reached equilibrium. Figure 1 displays the time evolutions of the 3D phase-separated structures at three annealing periods, matching those of the structures during

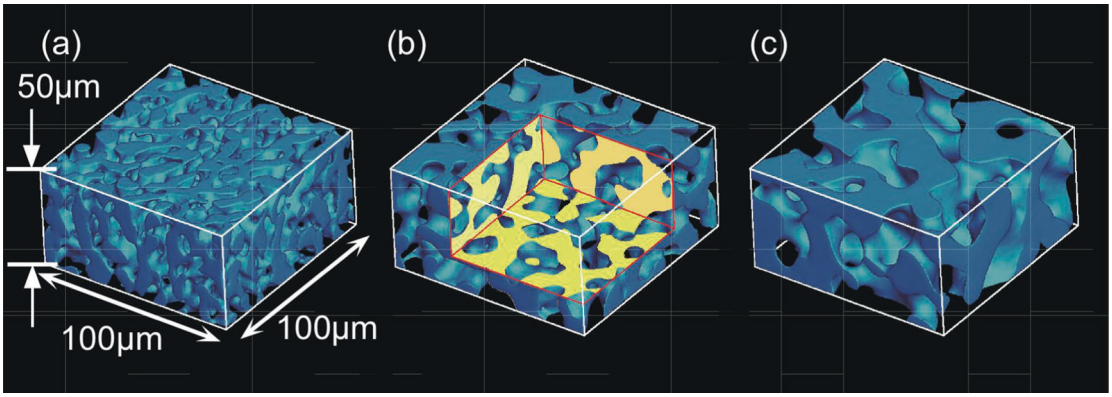

Fig. 1 LSCM figures indicating the time development of bicontinuous structures for the DPB/PB blend at a critical composition. The $100 \times 100 \times 50\,\mu m^3$ images were obtained (**a**) 1675, (**b**) 2880, and (**c**) 4860 min after the onset of SD at 40 °C. The figures only show the fluorescence-labeled PB-rich phase, as the DPB-rich one is transparent. Some portion of the structure in **b** was expelled to demonstrate a cross-section of the 3D structure. (Adapted with permission from H. Jinnai et al. *Langmuir* **16**, 4380–4393. Copyright (2000) American Chemical Society)

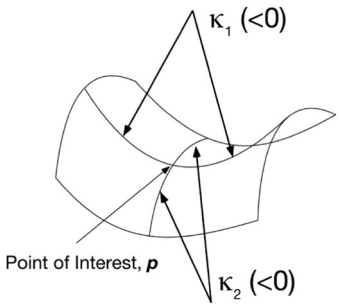

Fig. 2 Meaning of surface curvatures. The strong line at a point of interest, p, is a planar-beaded path. The chief bends at p are characterized as the maximum and minimum curvatures. Note that the curvature is signed; that is, the curvature is positive when the center of the curvature radius is placed on one side and negative when placed on the other side. The mean curvature, H, and the Gaussian curvature, K, are defined by Eq. (1). (Reprinted with permission from Y. Nishikawa et al. *Langmuir* **14**, 1242–1249. Copyright (1998) American Chemical Society)

late-stage SD. It also shows the bicontinuous and interpenetrating nature of the phase-separated structure.

Curvature distribution measurements

Two principal curvatures, the mean and Gaussian curvatures, reflect the curvatures at an arbitrary point on a surface [31]. Figure 2 schematically defines a planar-curved path passing through a point of interest (POI) on the surface from which the two principal curvatures, that is, κ_1 and κ_2 are defined [30].

The mean curvature, H, and the Gaussian curvature, K, are defined as,

$$H = \frac{\kappa_1 + \kappa_2}{2}, \quad K = \kappa_1 \kappa_2. \tag{1}$$

They are determined at point p. K refers to the surface contour, which is elliptic, parabolic, or hyperbolic when $K > 0$, $=0$, or <0, respectively. Two computational methods founded on differential geometry are used to determine the local curvatures from 3D images [32, 33]. One entails measuring surfaces areas parallel to the interface from which the mean area, $\langle H \rangle$, and Gaussian, $\langle K \rangle$, curvatures may be determined (not shown here) [32]. The other involves measuring curvature distributions determined by calculating curvatures at several points on the interface [33]. Although the former, called the "parallel surface method," is simple, it only provides area-averaged curvatures. Although the latter, called the "sectioning and fitting method" (SFM), demands heavy computational power, it contrastingly offers abundantly detailed information about interfacial shapes [33].

Curvature distribution measurements of phase-separating bicontinuous structures

Since SFM renders local surface curvatures at specific points on a surface, the joint probability density, $P(H, K;t)$, at any given time, t, may be determined. Figure 3 shows $P(H, K;t)$ of the DPB/PB mixture at $t = 1675$ min, which has an attribute functional form: (i) The majority of the calculated points (more than 90%) lie in the $K < 0$ region, meaning that the bicontinuous interface is anticlastic. (ii) The probability of $K > 0$, corresponding to the elliptic surface, is small. Finally, (iii) the observed probability density fulfills the relation $K \le H^2$. From $P(H, K;t)$, the marginal probability densities of the mean curvature, $P_H(H;t)$, and the Gaussian curvature, $P_K(K;t)$, are calculated as follows:

$$P_H(H;t) \equiv \int P(H, K;t) \mathrm{d}K, \tag{2}$$

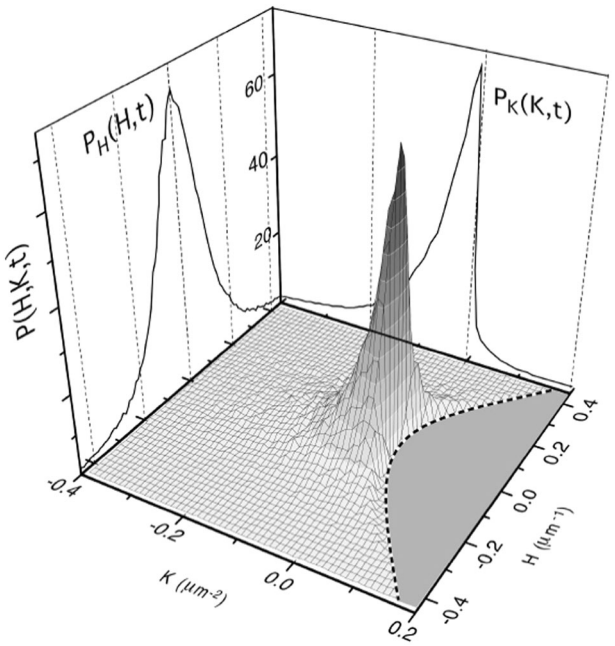

Fig. 3 Bird's-eye view of the joint probability density of a DPB/PB mixture at $t = 1675$ min. $P(H, K;t)$ was obtained by sampling ca. 2×10^5 randomly chosen surface points. Normally, the whole surface is comprised of approximately 2×10^6 surface foci. We guaranteed that the quantity of foci utilized for deciding $P(H, K;t)$ was satisfactory so that the state of the appropriation was invariant with additional testing. $P_H(H;t)$ and $P_K(K;t)$ are also shown. The discontinuous parabolic line shows $K = H^2$. (Reprinted with permission from H. Jinnai et al. *Langmuir* **16**, 4380–4393. Copyright (2000) American Chemical Society)

and

$$P_K(K;t) \equiv \int P(H,K;t)\mathrm{d}H. \tag{3}$$

Figure 4 demonstrates the time evolution of $P_H(H;t)$ and $P_K(K;t)$. $P_H(H;t)$ appears symmetric about $H = 0$, suggesting that the system follows the most reasonable low-free-energy evolution path during SD. The full-width at half-maximum of $P_H(H;t)$ diminished; subsequently, the portion of the distribution showing small $|H|$ increased with t. As mentioned above, $P_K(K;t)$ is distributed mostly in the $K < 0$ region, demonstrating again that the interface is hyperbolic regardless of t. The portion of small $|K|$ likewise increased as time elapsed [3]. The increments in the parts of $|H|$ and $P_K(K;t)$ propose an expansion in the normal range of curvature of the spinodal interface, that is, the interface moved toward becoming smoother with t .

Dynamic scaling analyses by the structural factor, $S(q/q_m, t)$ (q_m is the q at the scattering maximum), have been conducted many times. Several studies have highlighted the self-similar growth of the global structure, captured through

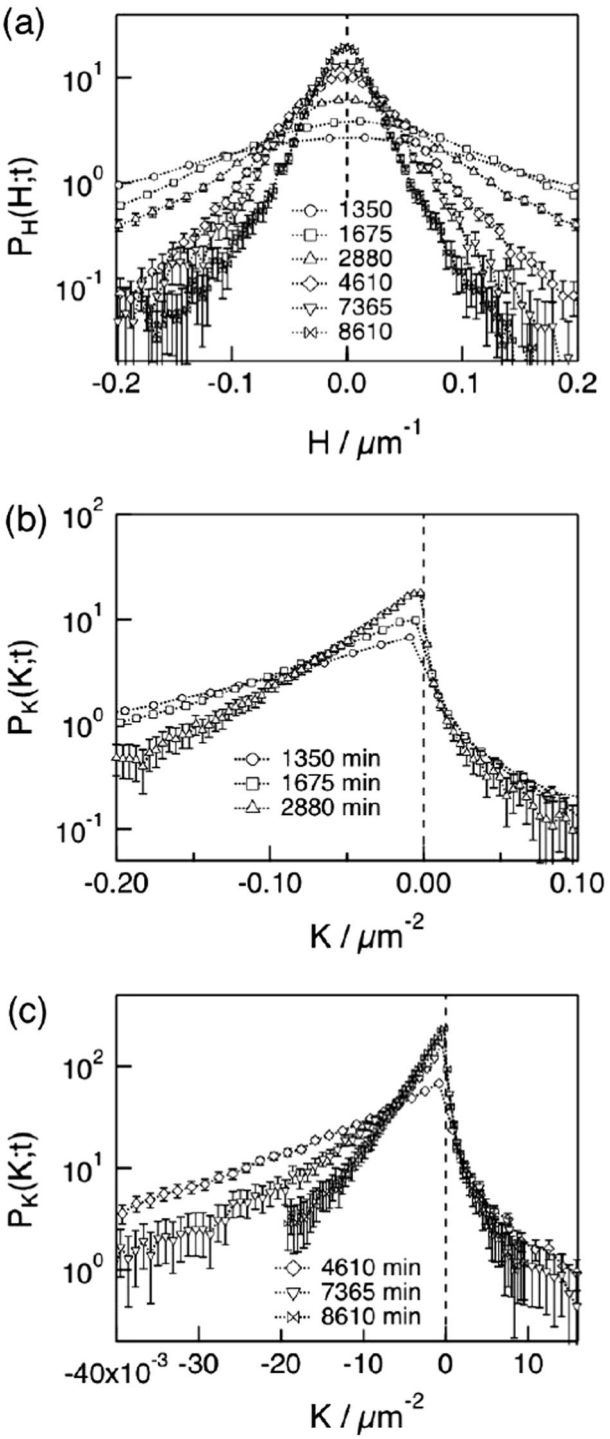

Fig. 4 Time evolution of **a** $P_H(H;t)$ and **b** $P_K(K;t)$ for the DPB/PB mixture during late-stage SD. (Reprinted with permission from H. Jinnai et al. *Langmuir* **16**, 4380–4393. Copyright (2000) American Chemical Society)

the scattering maximum, $\Lambda_m(t) \equiv 2\pi/q_m$. Whereas curvatures, reflected in the local shape of the structure, and $S(q, t)$ show an inherent relationship, which is not at all clear on a general level. Therefore, it is unclear whether the local

shape of the interface actually conforms to the dynamic scaling law.

To test the dynamic scaling law of the local structure, for instance, the curvature probability densities were determined through the interfacial area per unit volume, $\Sigma(t)$, along the length of the bicontinuous structures. The scaled probability densities of H, $\tilde{P}_H(\tilde{H};t)$, and K, $\tilde{P}_K(\tilde{K};t)$ are obtained by,

$$\tilde{P}_H(\tilde{H};t) = \Sigma(t)P_H(H;t), \quad \tilde{P}_K(\tilde{K};t) = \Sigma(t)^2 P_K(K;t). \tag{4}$$

Here, $\tilde{H} = H\Sigma^{-1}$ and $\tilde{K} = K\Sigma^{-2}$.

The scaled probability densities are plotted against t in Fig. 5. They fell nicely onto individual master curves both for H and K, demonstrating that the dynamic scaling law holds for interfacial curvatures as well. Figure 2 is remarkable because it shows the dynamic self-similarity of both the global structure and the local shape of the spinodal interface. Furthermore, the probability densities derived here should be universal to many condensed matter systems.

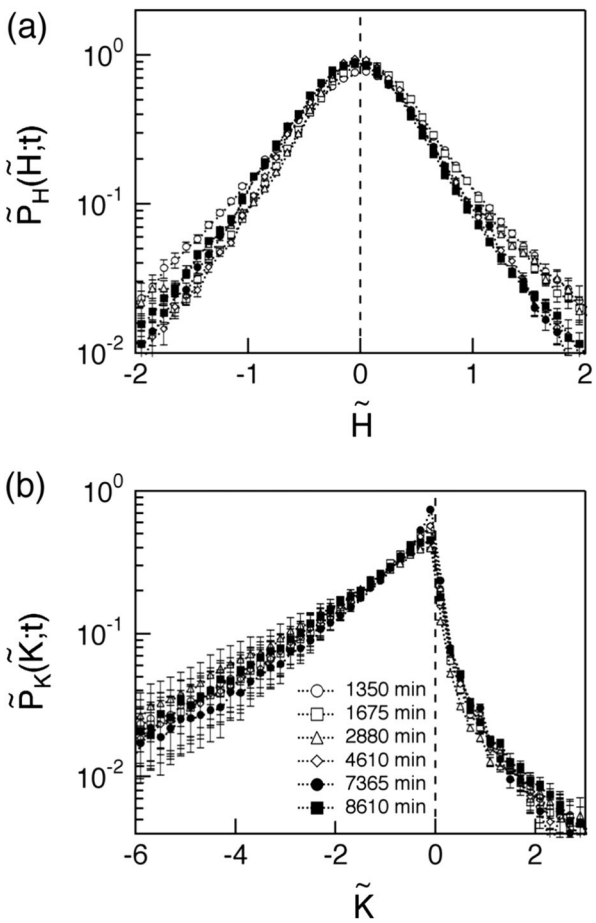

Fig. 5 Scaled probability densities **a** $\tilde{P}_H(\tilde{H};t)$ and **b** $\tilde{P}_H(\tilde{K}H;t)$ for the DPB/PB mixture in the late stage of SD. (Reprinted with permission from H. Jinnai et al., *Langmuir*, **16**, 4380–4393. Copyright (2000) American Chemical Society)

Dynamics of the spinodal interface

It is a fundamental question to investigate which aspects of spinodal interfaces are less stable and hence will change more rapidly during phase separation. Strictly speaking, the time evolutions of spinodally decomposing structures of exactly the same volume for a sufficiently small time interval should be studied to answer such a question. Although we did not follow the changes in morphology for the same observation volume, it is remarkable to examine the dynamics of spinodal interfaces vis-à-vis curvature-associated time changes. In this case, the time interval, $\Delta t = 2880 - 1675 = 1205$ min.

Since probability densities often vary, one may examine differences associated with such variations at two-phase separation times (1675 and 2880 min), that is, $\Delta P(H, K; \Delta t) \equiv P(H,K;t = 2880) - P(H, K;t = 1675)$. If Δt becomes infinitely small, $\Delta P(H, K;\Delta t)$ becomes $\partial P(H, K;t)/\partial t$. Depending on the sign of $\Delta P(H, K;\Delta t)$, one can determine the stability of the interface. Namely, if $\Delta P(H, K;\Delta t) < 0$, it means that the part of the interface at $t = 1675$ min decreases its frequency and will be changed (at $t = 2880$ min).

Figure 6 reveals a portion of the spinodal interface at $t = 1675$ min. The dots in Fig. 6 reveal unbalanced aspects of the spinodal interface conforming to negative $\Delta P(H, K; \Delta t)$. Part of the interface marked by circle "A" in Fig. 6 is an elliptic surface, as reflected by the positive Gaussian curvature. The mean curvature at this part of the interface was negative, meaning that it was curved inward relative to the DPB-rich domain and also that the pressure of the DPB phase was higher than that of the PB phase (based on the reasoning from the Laplace equation [34]). For the interface to relax such local pressure differences, the interface must be a planar surface so that $|H|$ decreases.

As marked by circles "B" and "C," other interfaces show negative K. Such interfaces show constricted shapes and a huge negative K, especially at the constricted part, "B" ("bridge"), where H was a relatively large positive number. Thus, the hyperbolic interface showed a larger principal radius of curvature, whose osculating circle center was located in the PB domain, than did the other interface. Such a cylindrical thread of fluid is unstable with regard to surface waves whose lengths exceed the cylinder circumference. The fluctuations in capillary waves gather capillary pressure gradients that move the thread, thereby forming fluid from thinner thread portions and eventually fragmenting into several spherical droplets arranged toward the thread. The bridge would be pinched off (like the interface marked by circle "C") owing to the capillary

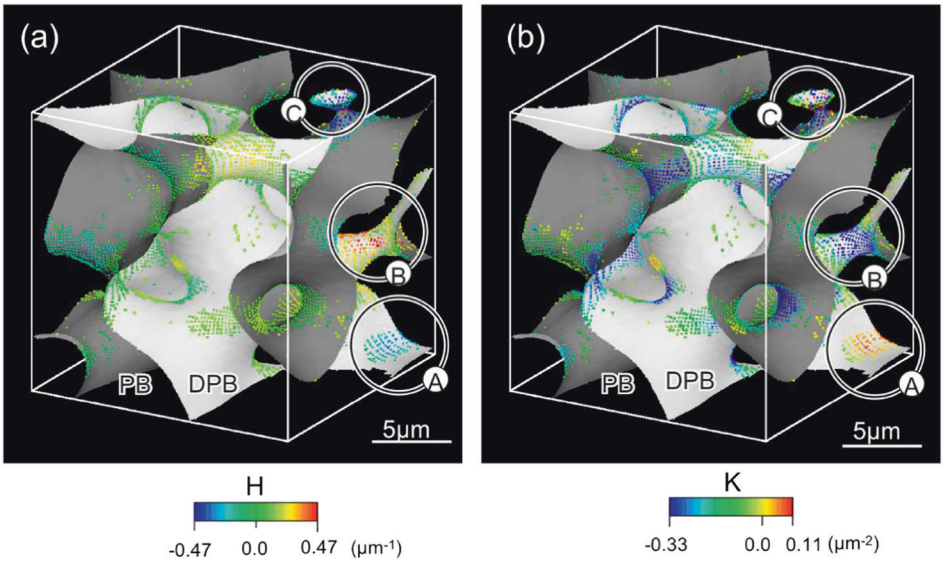

Fig. 6 Segment of DPB/PB blend spinodal interface at $t = 1675$ min (box estimate: $18.3^3\ \mu m^3$). The phase-separated domains facing the bright and dark sides of the interface are DPB and PB domains, respectively. The spots relate to the segment of the interface having $\Delta P(H, K;\Delta t) < 0$. Pseudocolors from red to blue indicate **a** the local mean curvatures in units of μm^{-1} and **b** the local Gaussian curvatures in units of μm^{-2} for the interface at $t = 1675$ min. The scale bar is 5 μm. The interface labeled "A" shows a part demonstrating a concave/convex surface becoming a flat surface with time. The circles marked "B" and "C" indicate "bridges" associating two nearby domains. These parts will break up during SD, thereby reducing the interface area. (Reprinted with permission from H. Jinnai et al. *Langmuir* **16**, 4380–4393. Copyright (2000) American Chemical Society)

pressure gradients. Once the bridge breaks up, it will split into a pair of elliptic surfaces, that is, corns, facing one another. The Gaussian curvature would abruptly turn positive, and the elliptic surfaces would become flat interfaces like the interface marked by "A." The curvature distribution should be a sensitive yardstick for assessing how phase separation works [30].

Interfacial morphologies of BCPs

BCPs show intermittent nanostructures as a result of the immiscibility between the different sequences [5, 6]. Some classical BCP nanostructures include A(B) spheres on body-centered cubic lattices in B(A) matrices, A(B) cylinders on hexagonal lattices in B(A) matrices, and coalternating lamellae. Of great interest is many complex (bicontinuous) nanostructure morphologies including HPL, DG, and DD [18, 35–39]. Figure 7 highlights a type of DG morphology observed using TEM. Such nanostructures may form amid cylindrical and lamellar morphologies when the copolymer composition, f, develops in a narrow range.

As mentioned in the first section, complex nanostructures like those in BCPs form in surfactants and lipids as a result of surface development with the CMC, which reduces interactions amid immiscible molecules [40]. The fact that BCP nanostructures have similar features has led to the emergence of the concept of CMC minimal surfaces [18] to explicate the stability of complex BCP nanostructures. On the basis of self-consistent field theory (SCFT), Matsen and Bates [41, 42] have averred that the area-averaged mean curvature, $\langle H \rangle$, and σ_H are significant factors when discussing the stability. Despite their apparent importance, neither $\langle H \rangle$ nor σ_H has been experimentally evaluated. TEMT is one of the best methods (and could be the only one) to measure surface curvature. The classic study by Spontak et al. [43] has led to the use of TEMT for the direct visualization and structural determination of complex BCP morphologies [44–72]. Although TEMT is a very potent microscopy technique for studying complex nanostructures, technical issues limiting full object rotation makes it less quantitative. Kawase et al. [73] have demonstrated that a rod-shaped polymer-nanocomposite-derived specimen can be fully quantitatively measured by completely rotating the specimen. They have also noted that reasonably accurate quantitative measurements, for example, a 10% error in the volume of one of the BCP constituents, can be achieved using a conventional 150-nm-thick plate-like specimen in the ±70° tilt range.

Direct visualization of a bicontinuous interface gyroid

This section describes the use of a poly(styrene-*block*-isoprene-*block*-styrene) (SIS) triblock copolymer. The experimental details and TEMT measurements have been well reported in the literature [44, 74, 75].

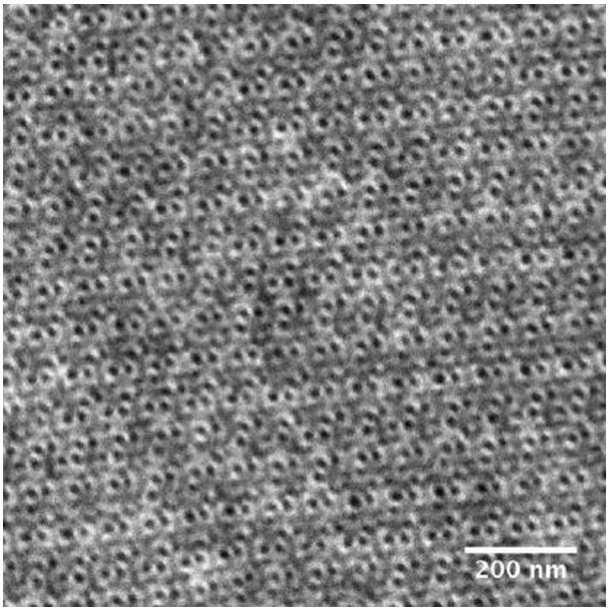

Fig. 7 TEM micrograph of a poly(styrene-*block*-isoprene) diblock copolymer. Attributable to recoloring, isoprene-rich areas are electron opaque and appear dark. Highly periodic nanostructures are shown

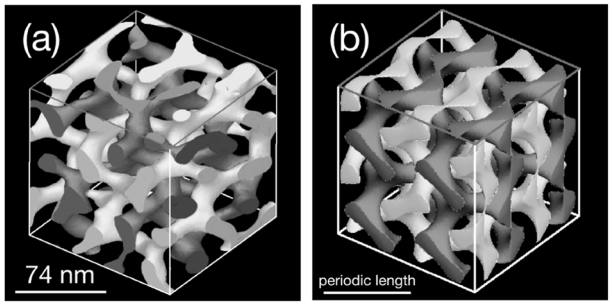

Fig. 8 **a** Transmission electron microtomograph of an SIS triblock copolymer DG morphology. **b** The corresponding CT model based on a Schoen gyroid surface. Nonintersecting light and dark channels relate to the minority microphase (PS in the SIS copolymer), while the majority part (PI) microphase is transparent. The edge of each cube is twice the periodic length, and the top cross-section recognizes the (001) plane. The lattice constants (**a**–**c**) of this nanostructure are $a =$ 78 nm, $b = 71$ nm, $c = 74$ nm, respectively. (Reprinted with permission from H. Jinnai et al. *Phys. Rev. Lett.* **84**, 518–521. Copyright 2000 by the American Physical Society)

Figure 8a shows a reconstructed 3D image of the microphase-separated SIS triblock copolymer nanostructure. The evident light and dark networks in Fig. 8a both reflect the PS microphase. They are distinctly shaded to show that the two PS channel networks never interconnect. The PI microphase is transparent to ensure clarity. The crystallographic analysis of the SIS triblock copolymer reveals that the microphase-separated nanostructure shows DG morphology.

Figure 8b shows a model bicontinuous morphology generated from the Schoen G surface. The microphase-separated SIS copolymer nanostructure may be mirrored with the styrene volume fraction, $f_S = 0.33$, by forming a new model interface through interpretation of the Schoen G interface with its normals direction equidistant to all points [33]. The resultant morphology is an approximate model of the hypothetical CMC interface and serves as the constant-thickness model [37]. The 3D morphologies in Fig. 8 were subject to interfacial curvature distributions.

Displayed in Fig. 9 is a surface contour representation of the joint probability density, $P(H, K)$, of the DG morphology. The marginal probability densities of the mean and Gaussian curvatures, $P_H(H)$ and $P_K(K)$, respectively, are included [33, 76]. Figure 9 shows that a large portion of the interface (77%) has $K < 0$, showing that the two main curvatures (κ_1 andκ_2) have opposite signs, akin to those observed for the polymer blend shown in the second section. From Fig. 9 it can be qualitatively inferred that because H is not constant at all the interface points, the CMC representation does not accurately represent the DG morphology.

Figure 10a shows the interfacial curvature probability densities of the SIS copolymer DG morphology, while Fig. 10b shows those of the CT model surface. For comparison $P_H(H)$, $P_K(K)$, and $P(H, K)$ are scaled with respect to Σ in a similar manner as for the polymer blend:

$$\tilde{P}_H(\tilde{H}) = \Sigma P_H(H), \quad \tilde{P}_K(\tilde{K}) = \Sigma^2 P_K(K) \tag{5}$$

and

$$\tilde{P}(\tilde{H}, \tilde{K}) = P(H, K)\Sigma^3. \tag{6}$$

Here, $\tilde{H} = H\Sigma^{-1}$ and $\tilde{K} = K\Sigma^{-2}$. The evaluation of the scaled probability densities in Fig. 10a shows that a portion of $\tilde{P}(\tilde{H}, \tilde{K})$ for the SIS DG morphology possesses $\tilde{H}<0$ and $\tilde{K}>0$, hinting that the interface is elliptically curved inward with respect to the isoprene microphase. This interfacial concavity is not obvious from the CT model in Fig. 10b, in which nearly all the measured points possess $\tilde{K}<0$. Thus, the SIS copolymer DG morphology is significantly different from the mathematical DG surface.

Because interfacial tension is the factor dominating the structural formation in microphase-separated BCPs, Thomas et al. [18] have advanced the idea that complex microphase-separated nanostructures develop within BCPs aligned with area-minimizing surfaces. In contrast, Matsen and Bates [41, 42] have observed that a relevant but often neglected factor in BCP nanostructure stability is packing frustration [19]. In order for certain blocks to uniformly fill space, self-adjustment occurs at interfaces, thereby preventing blocks from overstretching. This makes interfaces veer from the CMC. In this case, σ_H provides a measure of

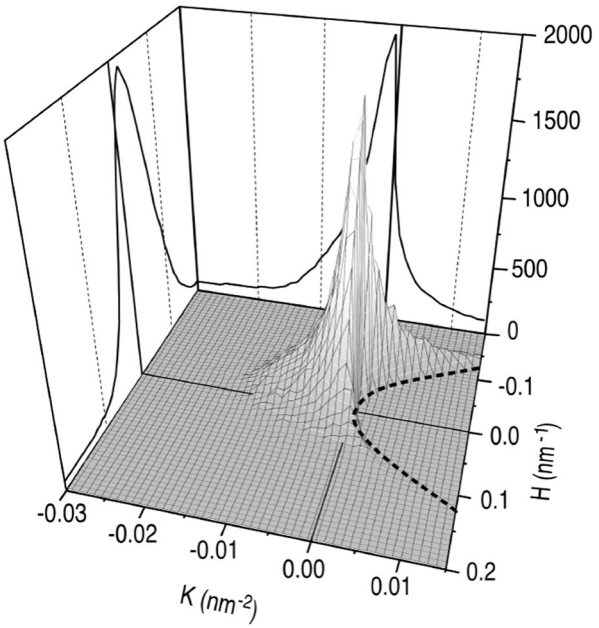

Fig. 9 Surface contour representation of the joint probability density, $P(H, K)$, measured from the SIS triblock copolymer DG morphology. The marginal probability densities, $P_H(H)$ and $P_K(K)$, are also shown. The dashed parabolic curve represents $K = H^2$. The curvature was arbitrarily chosen to be positive when the osculating circle center resides within the PI microphase. (Reprinted with permission from H. Jinnai et al. *Phys. Rev. Lett.* **84**, 518–521. Copyright 2000 by the American Physical Society)

the packing frustration and nanostructural stability. Although $\langle H \rangle$ and σ_H are predicted and are only obtainable for diblock copolymers [42], it is useful to relate the experimental interfacial curvatures generated in this report with the theoretical ones predicted by SCFT calculations.

The undisturbed statistical end-to-end distance of the SIS triblock copolymer, R_0, was estimated as 22 nm [76]. The probability densities derived for the DG morphology in the SIS copolymer yielded $\langle H \rangle = 0.034\,\mathrm{nm}^{-1}$ and $\sigma_H = 0.042\,\mathrm{nm}^{-1}$, which likewise can be represented as $\langle H \rangle = 0.74\,R_0^{-1}$ and $\sigma_H = 0.91 R_0^{-1}$. Assuming that the undisturbed chain length, R_0, does not vary, $\langle H \rangle$ and σ_H from the DG morphology CT model are $0.92R_0^{-1}$ and $0.55R_0^{-1}$, respectively. According to SCFT predictions [42], for an AB diblock copolymer with $f_A = 0.34$, $\langle H \rangle = 0.70$ and $\sigma_H = 0.12$ at $\chi N = 20$. Here, χ represents the Flory–Huggins interaction parameter and χN is a measure of the copolymer segregation power. χN for the SIS triblock copolymer is approximately 64. Hence, $\langle H \rangle$ obtained from the probability densities in Fig. 10a for the SIS triblock DG morphology agrees reasonably with that predicted by the SCFT; however, the σ_H derived in this report was higher than that predicted by SCFT. This discrepancy is owing to noise or to an imperfect angular tilt range embedded within the TEMT reconstruction or, otherwise, to the huge difference in χN (Matsen and Bates [42] have predicted that σ_H should increase with increasing χN). The BCP molecular architecture, that is, triblock (in this work) vs. diblock (in theory), and BCP molecular and compositional distributions likewise could account for the discrepancy. Further analysis of these experimental parameters, which influence σ_H, is required to achieve a valid contrast between the experimental and theoretical results.

In addition to the DG morphologies described above, some complex BCP 3D structures have been studied using TEMT. Such examples include morphological studies of HPL [55] and DD [67] structures. In the case of HPL, the differentiation of AB-type and ABC-type stacking has been successfully carried out [55]. The stability and 3D morphology of DD structures have also been discussed in the literatures [67, 77–79]. Chu et al. [67] presented the first real-space observation of a thermodynamically stable DD structure in a syndiotactic poly(propylene-*block*-styrene).

Helical structures in ABC triblock terpolymer

A stimulating example of a complex morphology formed in BCPs is the twofold helical structure of polystyrene-*block*-polybutadiene-*block*-poly(methyl methacrylate) triblock terpolymer (SBM) [62]. Following the elucidation of the double-helical DNA structure [80], the helix has drawn attention because of investigations into its molecular structure [81–85]. In materials science, a significant volume of studies has focused on the artificial formation and regulation of helical structures [81–83, 86].

Depicted in Fig. 11 are TEM micrographs of the SBM triblock terpolymer. The parallel dark-gray regions are OsO_4-stained PB microdomains, while the white and light-gray regions may be poly(methyl methacrylate) (PMMA) or PS microdomains. As revealed by the TEM images, PS cylinders and PB helical microdomains are hexagonally packed within the PMMA matrix. It is important to point out that the SBM terpolymer does not have a chiral entity in the constituent blocks (i.e., they are achiral), while the other systems exhibiting similar helical structures have chirality of the chemical compounds that is considered to be the main driving force of the formation of a helical structures.

Figure 11a unmistakably indicates left-handed and right-handed twofold helical structures. In contrast to the research summary regarding the same triblock copolymer by Krappe et al. [81], the SBM triblock terpolymer has a "twofold" helical structure instead of a four-stranded one. Surprisingly, the number of left-handed and right-handed helical structures were similar. Although the structural sequence seems arbitrary in regards to the helical sense, it is possible that neighboring pairs take contrasting helical configurations. TEMT alone offers detailed features of helical structures.

Helical "mesostructures" are increasingly gaining popularity [85–88]. We note that various morphological controls such as pitch [89], number of helical domains [89],

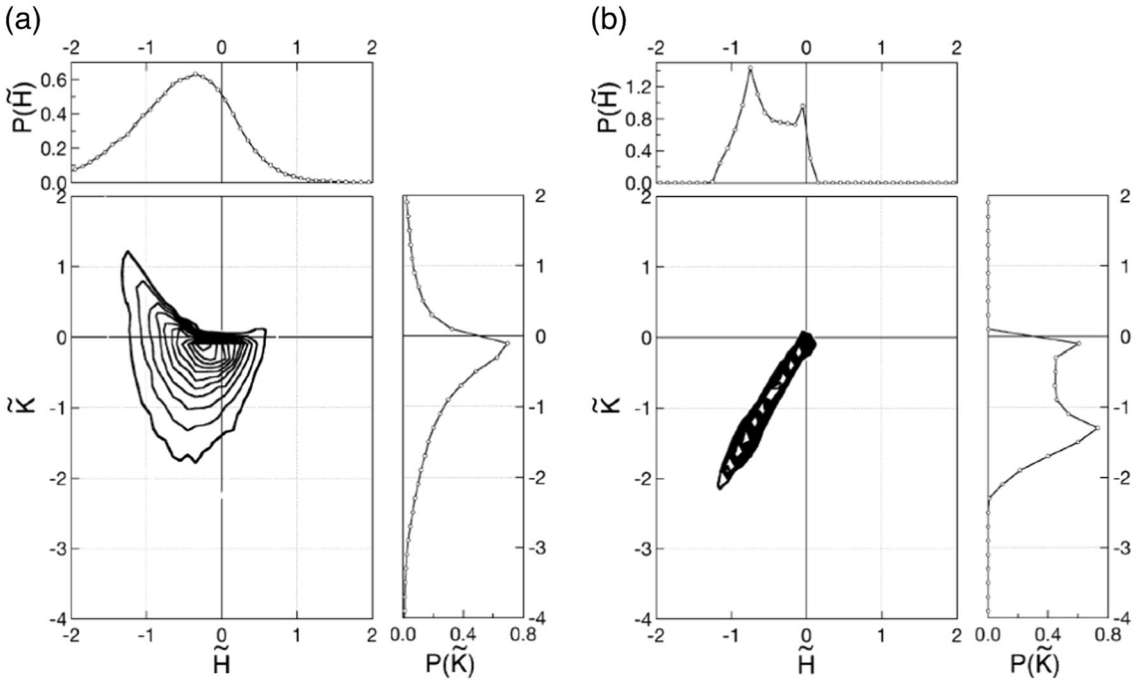

Fig. 10 Contour map of the scaled joint probability density, $\tilde{P}(\tilde{H},\tilde{K})$, and its marginal probability densities, $\tilde{P}_H(\tilde{H})$ and $\tilde{P}_K(\tilde{K})$, for **a** the SIS triblock copolymer DG morphology and **b** the G surface constant-thickness model. (Reprinted with permission from H. Jinnai et al. *Phys. Rev. Lett.* **84**, 518–521. Copyright 2000 by the American Physical Society)

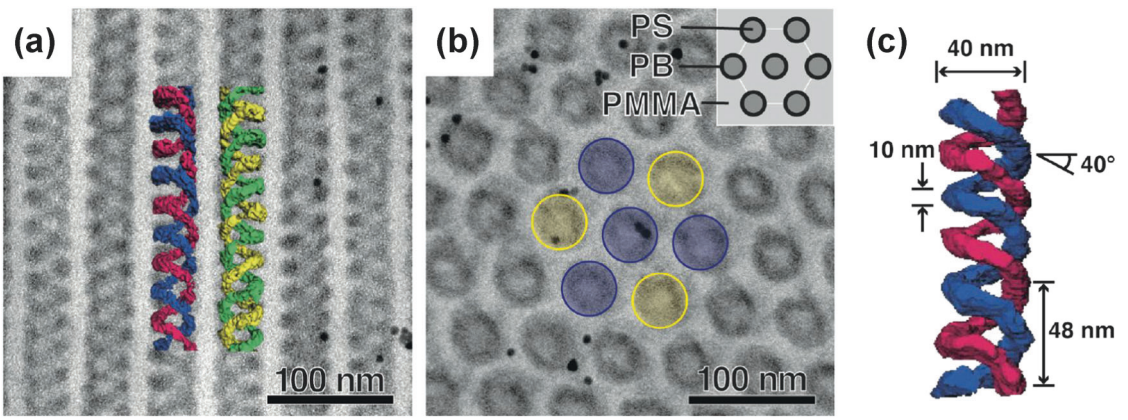

Fig. 11 TEM micrographs of an SBM triblock terpolymer demonstrating its two agent morphologies. OsO_4-recolored PB microdomains show up in black. **a**, **b** Two delegate shapes of the SBM terpolymer. Schematically appearing in the inset of **b**, the PS chambers and PB helical microdomains are hexagonally contained in the PMMA framework. 3D twofold helical structures appear at the highest point of the TEM picture in **a**. Left-handed and right-handed twofold helical structures appeared as blue-red and green-yellow helixes, respectively. The spatial arrangement of the left-handed and right-handed helixes are shown by blue and yellow circles, respectively, in **b**. **c** Structural measurements, for example, helix pitch, *d*, and helix distance across, *D*. TEM and TEMT 3D perceptions were completed utilizing a JEM-2200FS (JEOL Co., Ltd., Japan) operated at 200 kV. A series of TEM images were acquired at tilts in the range ±75° at 1° intervals. The experimental details can be found elsewhere in the literature [62]. (Reprinted with permission from H. Jinnai et al. *Macromolecules* **43**, 1675–1688. Copyright (2010) American Chemical Society)

orientation of helical structures on the substrates [63], and the incorporation of gold nanoparticles [70] have been demonstrated for the SBM terpolymer. Although control of the helical property has since not been reported for the SBM terpolymer, it has been demonstrated in other BCP polymers [90, 91].

3D interfacial morphology of complex local structure: grain boundaries

Although microphase-separated nanostructures are not as complicated as the DG and helical morphologies described in the previous sections, one can find complex BCP

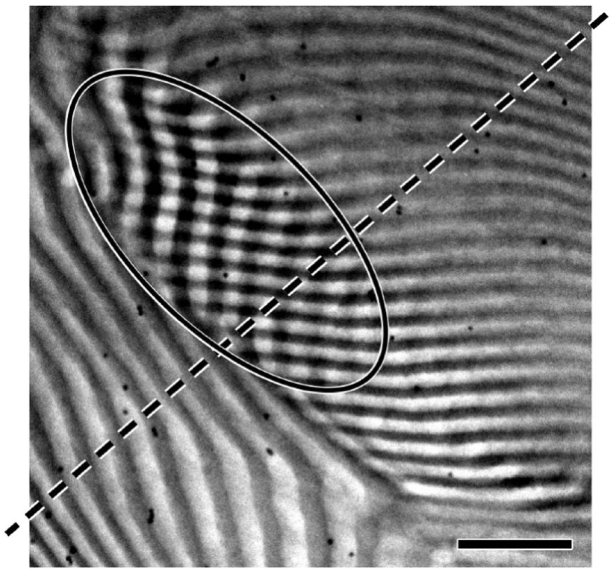

Fig. 12 TEM micrograph of an SI diblock copolymer. The contrasting domains correspond to PI and PS nanodomains. The dashed line represents an axis around which the region marked by the ellipsoid was tilted. The little dots are 5-nm-diameter Au nanoparticles. The scale bar designates 200 nm. (Reprinted with permission from H. Jinnai et al. *Macromolecules* **39**, 5815–5819. Copyright 2006 American Chemical Society)

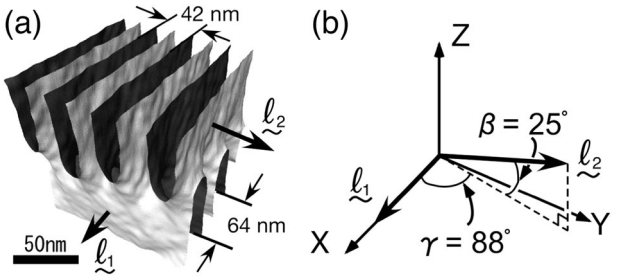

Fig. 13 **a** Surface-rendered 3D image of a grain boundary in an SI diblock copolymer. The interface is colored gray on one side and white on the other. The nanodomain looking toward the gray side is the PI nanodomain, while the PS nanodomain is toward the white side. Lamellar normals of the upper and lower grains are displayed by arrows. The tilt and twist angles between the two lamellar grains are demonstrated in **b**, in which the normal of the lower lamella, ℓ_1, lies along the *X*-axis. (Reprinted with permission from H. Jinnai et al. *Macromolecules* **39**, 5815–5819. Copyright 2006 American Chemical Society)

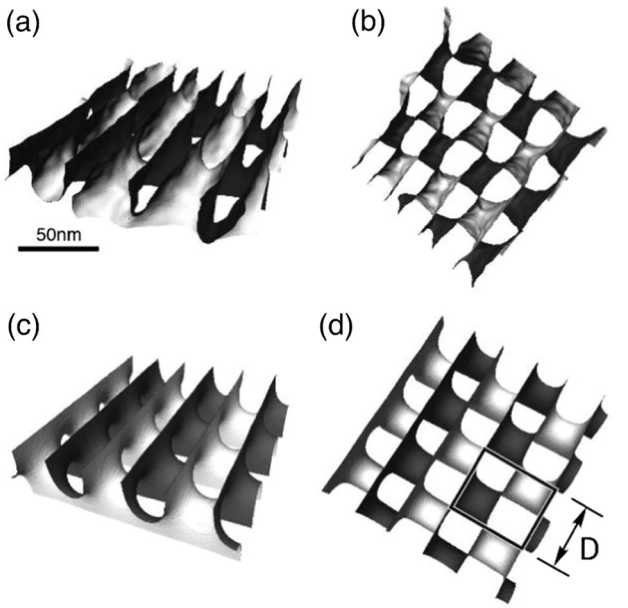

Fig. 14 Experimentally observed SI diblock copolymer grain boundary viewed from the **a** side and **b** top. Corresponding first Scherk surfaces are shown in **c**, **d**. In **d**, the bold boxed region shows the unit-cell top view. (Reprinted with permission from H. Jinnai et al., *Macromolecules*, **39**, 5815–5819. Copyright 2006 American Chemical Society)

morphologies. One such representative example is the boundary region between two adjacent grains. The morphology of boundary regions [92–94] amidst grains greatly influences the mechanical, electrical, and diffusional properties [95, 96] of BCPs. This is an "old" but somewhat "unsolved" problem in BCP morphological studies, where TEMT plays a critical role.

Although important, the 3D continuity of each microdomain at the grain boundary is nontrivial. As a problem in lamellar grain boundary morphology, the twist grain boundary (TGB) at which two lamellar nanodomains orthogonally converge remains unsolved. A 2D intermittent negligible surface, the principal Scherk surface, was once theorized as a model of such a grain limit morphology; however, it has only been tentatively discovered. Figure 12 presents a TEM micrograph of a poly(styrene-*block*-isoprene) (SI) diblock copolymer. As set apart by an ellipsoid, a crosshatched area normal to the TGB was observed.

Depicted clearly in Fig. 13a is the 3D surface-rendered image of the TGB. The upper and lower lamellar nanodomains intersect nearly perpendicularly. The lamellar normals are schematically shown by ℓ_1 and ℓ_2. ℓ_2 is aligned with the *X*-axis. The twist angle, γ, was 88°, within the TGB category—at least experimentally. The tilt angle, β, was 25°. Note that the ideal TGB has $\beta = 0°$.

Figure 14a, b show TEMT images of the TGB viewed from two different angles, while Fig. 14c, d show TEMT computer-generated first Scherk surfaces observed from directions similar to those in Fig. 14a, b, respectively. The first Scherk surface was generated using the following equation and the Cartesian coordinates (x, y, z) [92].

$$\exp z \cos x = \cos y. \tag{7}$$

The observed TGB appeared quite similar to the first Scherk surface (especially as shown in Fig. 14b, d). The area-averaged curvatures of the interface between the PI and PS microdomains and the interfacial area per unit volume

were determined experimentally. From these data, the experimentally obtained grain boundary morphology showed characteristics of a saddle-like hyperbolic surface quite similar to the first Scherk surface [51].

Single-chain conformation inside microphase-separated nanostructures

BCP subchains are packed into microdomains such that their chemical junctions are oriented at the interface. Although BCPs usually form highly periodic nanostructures, because of these topological constraints, the subchains are sometimes clumsily arranged in the nanodomains (i.e., "packing frustration") [41]. The morphology, then, is ultimately determined by the balance between subchain interaction (i.e., enthalpy) and subchain frustration (i.e., entropy). In the section "Direct visualization of a bicontinuous interface gyroid" and Fig. 10, the experimentally obtained and theoretically simulated DG interfaces are quantitatively compared based on the interfacial curvatures. Let us now consider this problem at the molecular level.

As a result of packing frustration stemming from chains deviating from their default conformations, attempts have been made to visualize bulk chain conformations [97–102] and chain conformations in restricted dimensions [103–105]. Small-angle neutron (or X-ray) scattering has been used to assess the gyration radii of subchains in lamellar-framing BCPs [97–100]. The results show that subchains laterally interpenetrate less than they interpenetrate normal to the interface. The obtained R_g is, however, an average, while it is inherently local. Different simulation techniques have been independently used to investigate the conformations of specific chains in nanodomains [106–108]. Aoyagi et al. [107], for instance, have evaluated the proportion of bridge to loop conformations in the lamellar domains of an ABA-type triblock copolymer using the SCFT [109–111] and coarse-grained molecular dynamics [106, 112] simulations. The triumph of their investigations shows that the degree of collaboration between experimental and simulation results may be enhanced.

Figure 15a shows a TEM micrograph of BCP lamellar morphology, and Fig. 15b, c correspond to 3D images obtained from the same BCP. The two cubes, A and B, demonstrated in Fig. 15c designate the areas assessed using 3D SCF simulations. The flat (A) and bent (B) lamellae correspond to the equilibrium lamellar morphology and the grain boundary, respectively. The experimentally obtained 3D interfaces were further used as the "boundary condition" for the SCF simulation, from which the subchain conformations were estimated [113]. The estimated R_g was consistent with the previous theoretical [109, 114] and experimental [99] results.

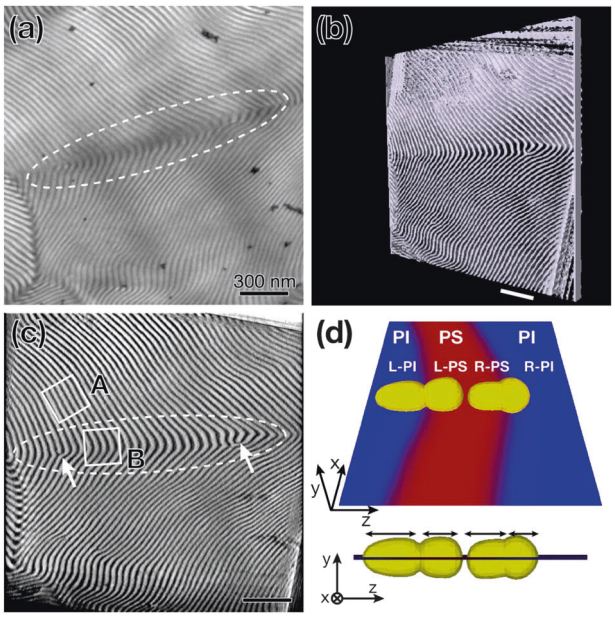

Fig. 15 Figures obtained by **a** TEM and **b**, **c** TEMT. The scale bars in each figure show 300 nm. The white broken lines in **a**, **c** demonstrate the boundary between two grains, while the squares in **c** show the areas contemplated utilizing SCF recreations. **d** Single-chain dimension in twisted lamellar spaces. The density of the PS fragments anticipated on the plane appears as a graded shading, and the appropriation of individual chains, $\phi_{\text{single}}(\mathbf{r})$, appear as the yellow shape. A JEM-1010 transmission electron microscope (JEOL, Co., Ltd., Japan) was operated at a 100 kV acceleration voltage. The pictures were obtained at tilts in the range ±60° in 2° increments. (Reprinted with permission from H. Morita et al. *Macromolecules* **41**, 4845–4849. Copyright 2008 American Chemical Society)

Shown in Fig. 15d is the outcome of the complete segment density distribution, $\phi_{\text{single}}(\mathbf{r})$, of the PS subchain at the bent lamellar interface. The isodensity surface corresponding to a specific $\phi_{\text{single}}(\mathbf{r})$, in turn corresponding to the "shape" of the PS subchain, is shown as a yellow surface. Interestingly, the PS subchain of the right-hand side chain appears more stretched than that of the left-hand side chain, probably as a result of interfacial curvature. In this area, the subchains are subjected to an extending or packing power emerging from the additional SCF angle because of interfacial arching. Thus, by combining TEMT and computer simulation, localized subchain conformations can be analyzed at particular points in the real domain. This method should foster a better understanding of the self-assembled nanostructures while enhancing materials science.

Dynamic processes in BCPs

As shown using some examples in the previous section, TEMT does not require any conventional preconditions to acquire 3D images. Indeed, the first two examples described in the section "Interfacial morphologies of block

copolymers" show that TEMT is a very potent tool for investigating "static" polymer nanostructures. Nevertheless, 3D "snapshots" may be employed in some situations to investigate dynamic processes of polymer nanostructures.

Order–order transition in BCPs

BCPs undergo OOTs, which are usually epitaxially associated with two-phase morphologies [20, 21, 23, 36, 55, 115–117]. A profoundly investigated example is the OOT from or to the DG structure, which is significantly more fascinating than other OOTs owing to the structural complication of the DG phase.

Figure 16 displays digitally cut TEMT and TEM images of a DG/hexagonally packed cylinder (HEX) SI–copolymer transition structure [60]. Figure 16b clearly shows the grain boundary between coexisting DG and HEX phases. HEX cylinders are placed laterally to the *X*-axis, while the $\{111\}_{DG}$ plane is clear. To better comprehend the 3D nanostructural morphology of the coexisting DG and HEX phases, many digitally cut images were derived from the hexahedral cross-section. Figure 16e displays an image of the HEX phase oriented perpendicular to the cylinder axis and an image of the $\{220\}_{DG}$ plane oriented orthogonal to both the $\{121\}_{DG}$ and $\{111\}_{DG}$ planes. The results show that the HEX cylinder axis is perpendicular to the $\{220\}_{DG}$ plane and parallel to both the $\{121\}_{DG}$ and $\{111\}_{DG}$ planes, as evident in Fig. 16c, d. Figure 16c shows the coexisting $\{10\}_{HEX}$ and $\{121\}_{DG}$ planes. Figure 16d is a magnified version of the image in Fig. 16b; the former clearly

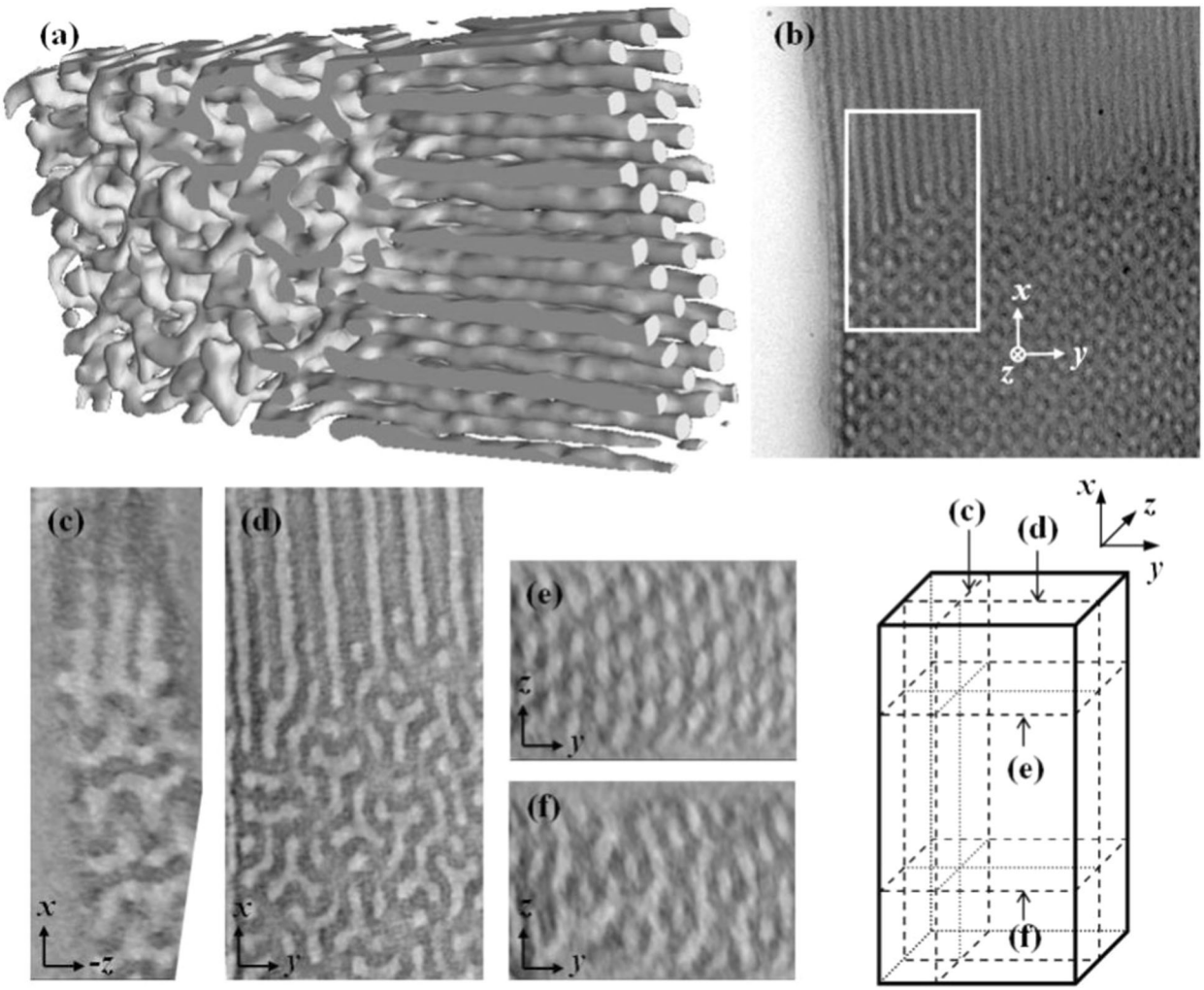

Fig. 16 **a** 3D reconstructed image of coexisting G and HEX structures. The hexahedron is 400 × 200 × 80 nm (*X*, *Y*, *Z*). Here, *Z* is the direction of the incident electron beam, and *X*–*Z* is the film plane (i.e., substrate surface). Only the PS domain is represented. **b** A TEM image of the sample region from which 3D image was reconstructed (boxed area). **c**–**f** Illustrated cross-sectional hexahedron figures. The polyisoprene (PI) block was stained with OsO_4 and appears darker. TEM and TEMT 3D images were obtained using a JEM-2200FS (JEOL Co., Ltd., Japan) operated at 200 kV. The details can be found elsewhere in the literature [60]. (Reprinted with permission from H.-W. Park et al. *J. Am. Chem. Soc*. **131**, 46–47. Copyright 2009 American Chemical Society)

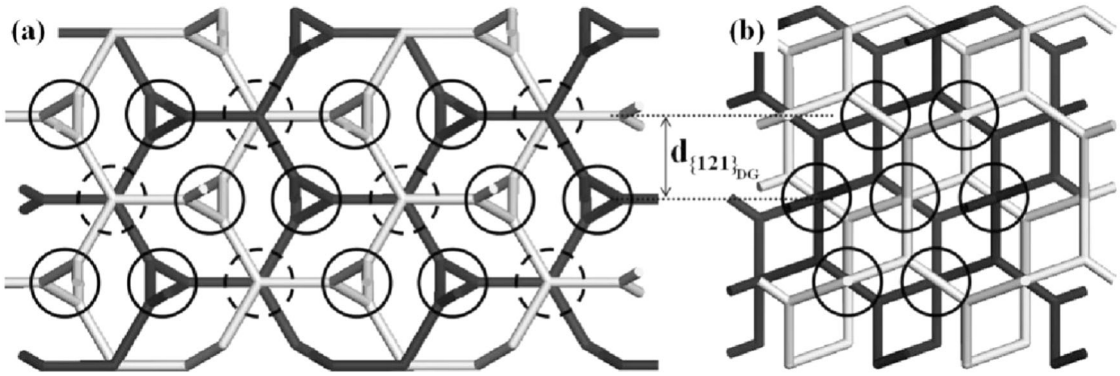

Fig. 17 **a** Simulated projection along $\langle 111\rangle_{DG}$. The two individual gyroids are represented by various dark tones. The two different types of cylinder axis loci are represented by solid and dotted circles. **b** Simulated projection along $\langle 220\rangle_{DG}$. The cylinder axis loci are represented by circles. In the $\langle 220\rangle_{DG}$-oriented cylinder axis development mechanism, all the loci are identical. (Reprinted with permission from H.-W. Park et al. *J. Am. Chem. Soc.* **131**, 46–47. Copyright 2009 American Chemical Society)

demonstrates the coexisting $\{11\}_{HEX}$ and $\{111\}_{DG}$ planes. Thus, the evidence clearly shows that the $\{121\}_{DG}$ and $\{111\}_{DG}$ planes had transitioned into the $\{10\}_{HEX}$ and $\{11\}_{HEX}$ ones, respectively. This type of epitaxial transition path has not been previously observed.

Matsen [20] has simulated the OOT between DG and HEX phases and proposed a plausible mechanism for how it occurs. The $\langle 111\rangle_{DG}$ axis is converted to the "side-on" HEX cylinder axis. As depicted in Fig. 17a, the estimated OOT along the $\langle 111\rangle_{DG}$ path shows a threefold symmetry, and the loci corresponding to the emerging HEX cylinder axes (shown by small circles) are not structurally even but are of two distinct types (shown by solid and dotted circles in Fig. 17a). Tripodal skeletons of two individual gyroids must be joined to form a HEX cylinder at the loci shown by the dotted circles.

Governed by the transitional mechanism described in this section, HEX cylinders are laterally molded in the $\langle 220\rangle_{DG}$ direction (i.e., "head-on"). As shown in Fig. 17b, the symmetry of the $\{220\}_{DG}$ projection is marginally misshapen from the hexagon on the right. In contrast to how the cylinder axis develops along the $\langle 111\rangle_{DG}$ path [20, 23, 118], the cylinder axis will instead develop through the joining of two individual gyroid skeletons because all the loci are topologically equivalent [60]. Although the emerging hexagon is somewhat distorted, the $\{121\}_{DG}$ plane will transition to the $\{10\}_{HEX}$ plane without any agitation. Interestingly, the OOT path inversion, that is, from HEX to DG, will lead to side-on epitaxy and head-on relationships [119].

One of the marked properties of the aforementioned OOTs is that they occur in thin films. The surface interactions of BCPs tend to have a greater influence on phase transitions in a thin films than they do in bulks. How the OOT behaves in a thin films as opposed to in bulks has already been studied. Park et al. [55] have shown that in phase transitions of HPLs, DG and HPL layers developed along the $\{121\}_{DG}$ plane in thin films; while in the phase transitions of shear-oriented bulks, the layers do not show any such methodical conversion [115, 116]. Furthermore, HPL layers may connect to the $\{111\}_{DG}$ plane in the DG/HPL bulk grain boundary structure [120], which is not well suited to the epitaxially associated HPL layers and the $\{121\}_{DG}$ plane in thin films [55]. Hence, the BCP OOTs require additional investigation. TEMT is therefore critical because it renders epitaxial relationships between preexisting and newly formed microdomains as well as processes for rearranging microdomains [60, 118, 121].

Recent developments in electron microscopy toward in situ 3D observations of dynamic processes

As discussed in the previous section, altering the temperature or pressure or applying an external field structurally changes BCP nanostructures. OOTs are analyzed by first freezing specimens and then observing boundary structures between extant and freshly formed nanostructures. In the OOT between DG and HEX structures, two epitaxial phase transition paths exist based on the OOT path. Understanding such complex processes requires the ability to conceive structural changes in situ over time.

Developing time-dependent 3D nanoimaging is the epicenter of several studies. In the field of lanthanides, for example, ultralow-dose electron tomography showing a 3.5-s temporal resolution has been demonstrated [122]. Because dynamic processes in polymers are often slow, the required resolution falls within the order of minutes. An inherent obstacle to in situ analysis is that samples usually must be first stained to enhance contrast under the electron beam, whereas, although staining is usually operational in TEM polymer structural observations [123], it may mar in situ dynamic imaging. In addition, staining may slightly alter morphologies [68].

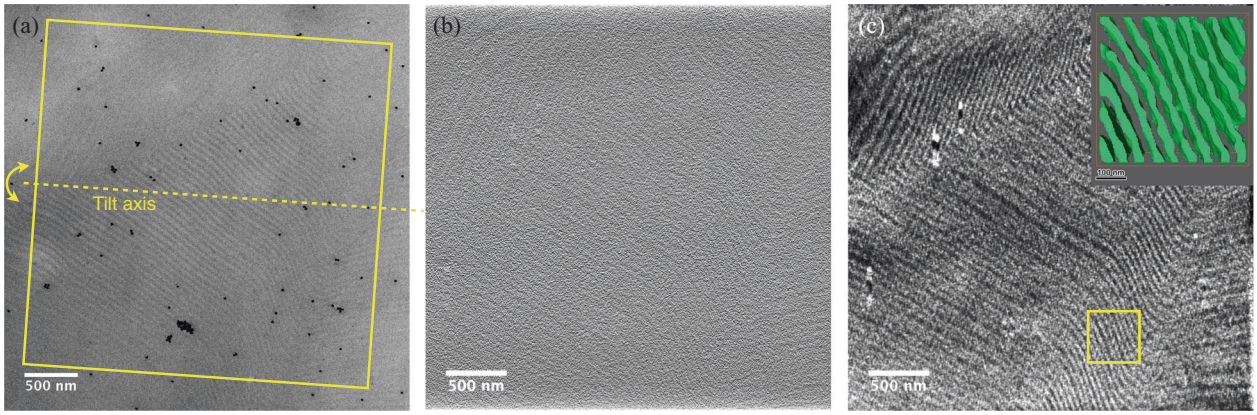

Fig. 18 **a** STEM picture of an unstained SI BCP acquired utilizing an accelerating voltage of 200 kV and a convergence angle of 6.8 mrad. Electrons scattered up to 14.5 mrad were utilized to create the 2D STEM picture. **b** Digitally cut pictures recreated in the locale encased by the yellow square in **a** by **b** FBP and **c** TVR-DART calculations. The inset shows the 3D structures of PI phases visualized from the yellow square in **c**. (Reprinted with permission from H. Jinnai et al. *Acc. Chem. Res*. **50**, 1293–1302. Copyright 2017 American Chemical Society)

Therefore, as a means of enhancing contrast, therefore, STEM has been put forward [124]. It is possible to enhance contrast owing to small variations in density among polymers by using a relevant combination of electron beam convergence and scattered electron detection angles in STEM. Other approaches to enhancing contrast, such as phase plates and differential phase contrast (S)TEM, are appropriate for polymers [125].

Figure 18a shows a STEM image from the lamellar microphase-separated nanostructure of an unstained SI, where the higher density PS and lighter PI microdomains appear as dark and light, respectively [126]. A 3D STEM image was then captured for the unstained BCP. The area marked by the yellow square in Fig. 18a was tilted around the axis shown by the dotted line. A total of 25 STEM projections were captured at tilts in the range ±60° in 5° increments. The projection volumes were markedly smaller than those captured in traditional TEMT experiments as a result of the marked increase in electron beam-induced damage to the unstained specimen.

3D images were rebuilt through a conventional filtered back projection [127] based on fewer STEM projections from the unstained SI BCP sample. One such digitally cut (or sliced) image is displayed in Fig. 18b. The lamellar microdomains were barely identifiable. Although Zhuge et al. [128, 129] have recently shown that only 21 projections captured over a 60° tilt range are required in order to gain a fairly valid 3D reconstruction based on their total variation regularized discrete algebraic reconstruction (TVR-DART) technique, however, the technique requires foreknowledge of the amounts of the materials in a specimen. Figure 18c shows the image reconstructed by TVR-DART and digitally sliced at exactly the same position as the reconstructed image shown in Fig. 18b. Clearly, the two reconstructed images show some distinct variations; the lamellar microdomains are readily identifiable in the TVR-DART reconstructed image but not in the digitally cut STEM image shown in Fig. 18b. Hence, a combination of these two recent breakthroughs (i.e., the contrast enhancement using STEM and the new image reconstruction algorithm) should lead to novel vistas for 3D in situ real-time polymer structural analysis.

Concluding remarks

This paper has reviewed the interfacial morphologies and associated dynamic processes of multicomponent polymers, emphasizing multiscale 3D microscopy observations and analysis. For now, TEMT, LSCM, and high-resolution X-ray CT (not shown here) are extant. Although LSCM and X-ray CT are valuable for imaging microstructural morphologies, TEMT employs tomography using the TEM. As such, it is useful in obtaining 3D images of phase-separated nanostructures or even smaller structural morphologies.

From the 3D volume data array obtained by 3D microscopes, some basic structural parameters, for example, the constituent volume fractions, ϕ, and interfacial volume per unit volume, Σ, can be directly measured. Apart from the information regarding these basic structural properties, the 3D digital data array is also rich in structural information, extractable by quantitative and advanced image analyses. The evaluation of new parameter sets including some topological measures and interfacial curvatures, for example, the connectivity of network domains and surface genus, is also feasible. It is worth emphasizing that these structural properties are hardly ever assessed using other experimental protocols.

With the aid of these 3D microscopy techniques, the essential aspects of the stability and dynamics of

multicomponent polymers have been unveiled. In polymer blends, the time evolutions of spinodally decomposing interfaces were directly observed, and the two elementary interface dynamics occurring during phase separation were observed for the first time. The interfacial morphology scalability was critically tested and found valid both locally and globally. For the application of TEMT to BCP morphologies, highly complex interfacial morphologies, for example, the double-gyroid morphology of the ABA-type BCP and the double-helical morphology of an ABC-type triblock terpolymer were observed for the first time. Molecular level information, including the packing frustration of blocks in microphase-separated nanostructures, was quantitatively discussed using 3D images and advanced image analysis based on computer simulation.

Dynamic nanoprocesses such as the OOT in BCPs can be very precisely studied using TEMT. Namely, TEMT is valuable for directly rendering images and dynamic and static nanostructural information. However, it would be ideal if we could directly observe such dynamic nanoprocesses in situ, which is difficult to accomplish with polymer samples because staining them for contrast enhancement may fix and alter their morphology and because the electron beam damages them. Thus, these represent the two major challenges thwarting the advent of in situ electron tomography for polymer materials. A new electronic optics method effectively generated adequate contrast for TEM even without staining, and a novel 3D image reconstruction algorithm enabled high-contrast, quantitative 3D image rendering using fewer projections than are needed in conventional image-rendering processes, thereby minimizing the electron dose to the polymer samples. A combination of these novel approaches should give rise to new vistas for 3D in situ real-time polymer structural analysis.

Acknowledgements This work was partially supported by JSPS KAKENHI (grant no. 16H02288) Japan. We deeply appreciate all the collaborators for their helpful discussions and supports. HJ is grateful to Prof. Takeji Hashimoto, Prof. Toshio Nishi and Prof. Charles C. Han for their guidance. We thank the editorial support in the form of writing provided by Editage.

Compliance with ethical standards

Conflict of interest The authors declare that they have no conflict of interest.

References

1. Hashimoto T. Structure of polymer blends, Vol. 12 of Materials Science and Technology. Weinheim: VCH; 1993.
2. Jinnai H, Nishikawa Y, Koga T, Hashimoto T. Direct observation of 3-dimensional bicontinuous structure developed via spinodal decomposition. Macromolecules. 1995;28:4782–4.
3. Jinnai H, Koga T, Nishikawa Y, Hashimoto T, Hyde ST. Curvature determination of spinodal interface in a condensed matter system. Phys Rev Lett. 1997;78:2248–51.
4. Lopez-Barron CR, Macosko CW. Characterizing interface shape evolution in immiscible polymer blends via 3D image analysis. Langmuir. 2009;25:9392–404.
5. Bates FS, Fredrickson GH. Block copolymers—designer of soft materials. Phys Today. 1999;52:32–38.
6. Abetz V, Simon PFW. Phase behavior and morphologies of block copolymers. Adv Polym Sci. 2005;189:125–212.
7. Gunton JD, Miguel MS, Sahni PS. The dynamics of first order phase transitions. Vol. 8. New York: Academic Press; 1983.
8. Snyder HL, Meakin P. Phase separation dynamics: comparison of experimental results. J Chem Phys. 1983;79:5588–94.
9. Izumitani T, Hashimoto T. Slow spinodal decomposition in binary liquid mixtures of polymers. J Chem Phys. 1985;83:3694–701.
10. Sato T, Han CC. Dynamics of concentration fluctuation in a polymer blend on both sides of the phase boundary. J Chem Phys. 1988;88:2057–65.
11. Wiltzius P, Bates FS, Heffner WR. Spinodal decomposition in isotopic polymer mixtures. Phys Rev Lett. 1988;60:1538–41.
12. Hashimoto T, Takenaka T, Jinnai H. Scattering studies of self-assembling processes of polymer blends in spinodal decomposition. J Appl Crystallogr. 1991;24:457466.
13. Schwahn D, Hahn K, Streib J, Springer T. Critical fluctuations and relaxation phenomena in the isotopic blend polystyrene/deuteropolystyrene investigated by small angle neutron scattering. J Chem Phys. 1990;93:8383–91.
14. Jinnai H, Hasegawa H, Hashimoto T, Han CC. Time-resolved small-angle neutron scattering in intermediate- and late-stage spinodal decomposition of DPB/HPI blends. Macromolecules. 1991;24:282–9.
15. Jinnai H, Hasegawa H, Hashimoto T, Briber RM, Han CC. Effect of cross-links on the miscibility of a deuterated polybutadiene and protonated polybutadiene blend. Macromolecules. 1993;26:182–8.
16. Jinnai H, Hasegawa H, Hashimoto T, Han CC. Time-resolved small-angle neutron scattering study of spinodal decomposition in deuterated and protonated polybutadiene blends. I. Effect of initial thermal fluctuations. J Chem Phys. 1993;99:4845–54.
17. Jinnai H, Hasegawa H, Hashimoto T, Han CC. Time-resolved small-angle neutron scattering study of spinodal decomposition in deuterated and protonated polybutadiene blends. II. q-dependence of onsager kinetic coefficient. J Chem Phys. 1993;99:8154–86.
18. Thomas EL, Anderson DM, Henkee CS, Hoffman D. Periodic area-minimizing surfaces in block copolymers. Nature. 1988;334:598–601.
19. Gruner SM. Stability of lyotropic phases with curved interfaces. J Phys Chem. 1989;93:7562–70.
20. Matsen MW. Cylinder ↔ gyroid epitaxial transitions in complex polymeric liquids. Phys Rev Lett. 1998;80:4470–3.
21. Wang C-Y, Lodge TP. Kinetics and mechanisms for the cylinder-to-gyroid transition in a block copolymer solution. Macromolecules. 2002;35:6997–7006.
22. Park I, et al. Epitaxial phase transition of polystyrene-*b*-polyisoprene from hexagonally perforated layer to gyroid phase in thin film. Macromolecules. 2005;38:10532–6.
23. Honda T, Kawakatsu T. Epitaxial transition from gyroid to cylinder in a diblock copolymer melt. Macromolecules. 2006;39:2340–9.
24. Hawker CJ, Wooley KL. The convergence of synthetic organic and polymer chemistriess. Science. 2005;309:1200–5.
25. Kamigaito M, Sato K. Stereoregulation in living radical polymerization. Macromolecules. 2008;41:269–76.

26. Percec V. Introduction to frontiers in polymer synthesis. Nat Chem. 2009;109:4961–2.
27. Matyjaszewski K, Tsarevsky NV. Nanostructured functional materials prepared by atom transfer radical polymerization. Nat Chem. 2009;1:276–88.
28. Momose A, Fujii A, Kadowaki H, Jinnai H. Three-dimensional observation of polymer blends by X-ray phase tomography. Macromolecules. 2005;38:7197–200.
29. Saito H, et al. Direct three-dimensional imaging of the fracture of fiber-reinforced plastic under uniaxial extension: effect of adhesion between fibers and matrix. Polymer (Guildf). 2017;116:556–64.
30. Jinnai H, Nishikawa Y, Morimoto H, Koga T, Hashimoto T. Geometrical properties and interface dynamics: time evolution of spinodal interface in a binary polymer mixture at the critical composition. Langmuir. 2000;16:4380–93.
31. Hyde S, et al. The language of shape. Amsterdam–Lausanne–New York–Oxford–Shannon–Tokyo: Elsevier; 1997.
32. Nishikawa Y, Jinnai H, Koga T, Hashimoto T. Measurements of interfacial curvatures of bicontinuous structure from three-dimensional digital images. 1. A parallel surface method. Langmuir. 1998;14:1242–9.
33. Nishikawa Y, Jinnai H, Koga T, Hashimoto T. Measurements of interfacial curvatures of bicontinuous structure from three-dimensional digital images. 2. A sectioning and fitting method. Langmuir. 2001;17:3254–65.
34. Adamson AW, Gast AP. Physical chemistry of surfaces. New York: Wiley; 1997.
35. Thomas EL, et al. Ordered bicontinuous double-diamond structure of star block copolymers: a new equilibrium microdomain morphology. Macromolecules. 1986;19:2197–202.
36. Schulz ML, Bates FS, Almdal K, Mortensen K. Epitaxial relationship for hexagonal-to-cubic phase transition in a block coplymer mixture. Phys Rev Lett. 1994;73:86–9.
37. Hajduk DA, et al. The gyroid: a new equilibrium morphology in weakly segregated diblock copolymers. Macromolecules. 1994;27:4063–75.
38. Hajduk DA, Ho R.-M, Hillmyer MA, Bates FS, Almdal K. Transition mechanisms for complex ordered phases in block copolymer melts. J Phys Chem B. 1998;102:1356–63.
39. Schick M. Avatars of the gyroid. Phys A. 1998;251:1–11.
40. Hyde ST, et al. The language of shape. Amsterdam: Elsevier science B. V.; 1997.
41. Matsen MW, Bates FS. Origins of complex self-assembly in block copolymers. Macromolecules. 1996;29:7641–4.
42. Matsen MW, Bates FS. Block copolymer microstructures in the intermediate-segregation regime. J Chem Phys. 1997;106:2436–48.
43. Spontak RJ, Williams MC, Agard DA. Three-dimensional study of cylindrical morphology in a styrene-butadiene-styrene block copolymer. Polymer (Guildf). 1988;29:387–95.
44. Spontak RJ, et al. Phase behavior of ordered diblock copolymer blends: effect of compositional heterogeneity. Macromolecules. 1996;29:4494–507.
45. Radzilowski LH, Carragher BO, I. S. Three-dimensional seli-assembly of rodcoil copolymer nanostructures. Macromolecules. 1997;30:2110–9.
46. Laurer JH, et al. Microstructural analysis of a cubic bicontinuous morphology in a neat sis triblock copolymer. Macromolecules. 1997;30:3938–41.
47. Jinnai H, et al. Topological similarity of sponge-like bicontinuous morphologies. Adv Mater. 2002;14:1615–8.
48. Yamauchi K, et al. Microdomain morphology in an ABC 3-miktoarm star terpolymer: a study by energy-filtering tem and 3D electron tomography. Macromolecules. 2003;36:6962–6.
49. Wilder EA, et al. Nanofibrillar networks in poly(ethyl methacrylate) and its sillica nanocomposites. J Phys Chem B. 2003;107:11633–42.
50. Xu T, et al. Electric field alignment of asymmetric diblock copolymer thin film. Macromolecules. 2005;38:10788–98.
51. Jinnai H, Sawa K, Nishi T. Direct observation of twisted grain boundary in a blook copolymer lamellar nanostructure. Macromolecules. 2006;39:5815–9.
52. Jinnai H, et al. 3D nanometer-scale study of coexisting bicontinuous morphologies in a block copolymer/homopolymer blend. Macromol Rapid Commun. 2006;27:1424–9.
53. Jinnai H, Yasuda K, Nishi T. Three-dimensional observations of grain boundary morphologies in a cylinder-forming block copolymer. Macromol Symp. 2006;245-246:170–4.
54. Kaneko T, et al. A "ladder" morphology in an abc triblock copolymer. Macromol Symp. 2006;242:80–86.
55. Park H-W, et al. Direct observation of HPL and DG structure in ps-*b*-pi thin film by transmission electron microscopy. Macromolecules. 2007;40:2603–5.
56. Miura Y, et al. Axbax-type block graft polymers with soft methacrylate middle segments and hard styrene outer grafts: synthesis, morphology, and mechanical properties. Chem Asian J. 2007;2:662–72.
57. Chen Y, et al. Perforated block copolymer vesicles with a highly folded membrane. Macromolecules. 2007;40:4389–92.
58. Yang X, Loos J. Toward high-performance polymer solar cells: the imprtance of morphology control. Macromolecules. 2007;40:1353–62.
59. Niihara K-I, et al. A transition from cylindrical to spherical morphology in diblock copolymer thin films. Macromolecules. 2008;41:9318–25.
60. Park H.-W, Jung J, Chang T, Matsunaga K, Jinnai H. New epitaxial phase transition between dg and hex in ps-*b*-pi. J Am Chem Soc. 2009;131:46–7.
61. Zhao Y, et al. Small molecule directed nanoparticle assembly toward stimuli-responsive nanocomposites. Nat Mater. 2009;8:979–85.
62. Jinnai H, Kaneko T, Matsunaga K, Abetz C, Abetz V. A double helical structure formed from an amorphous, achiral abc triblock terpolymer. Soft Matter. 2009;5:2042–6.
63. Hong S, et al. Highly oriented and ordered double-helical morphology in ABC triblock terpolymer films up to micrometer thickness by solvent evaporation. Polym J. 2012;44:567–72.
64. Hanisch A, et al. Counterion-mediated hierarchical self-assembly of an ABC miktoarm star terpolymer. ACS Nano. 2013;7:4030–41.
65. Li Z, et al. Linking experiment and theory for three-dimensional networked binary metal nanoparticle-triblock terpolymer superstructures. Nat Commun. 2014;5:3247.
66. Wong M, et al. Large-scale self-assembled zirconium phosphate smectic layers via a simple spray-coating process. Nat Commun. 2014;5:3589.
67. Chu CY, et al. Real-space evidence of the equilibrium ordered bicontinuous double diamond structure of a diblock copolymer. Soft Matter. 2015;11:1871–6.
68. Ishige R, et al. Structural analysis of microphase separated interface in an ABC-type triblock terpolymer by combining methods of synchrotron-radiation grazing incidence small-angle X-ray scattering and electron microtomography. Macromolecules. 2015;48:2697–705.
69. Mineart KP, Jiang X, Jinnai H, Takahara A, Spontak RJ. Morphological investigation of midblock-sulfonated block ionomers prepared from solvents differing in polarity. Macromol Rapid Commun. 2015;36:432–8.
70. Higuchi T, Sugimori H, Yabu H, Jinnai H. Controlled incorporation behavior of gold nanoparticles into ABC triblock

terpolymer with double-helical morphology. Polym J. 2016;48: 509–15.
71. Guerin G, et al. Lateral growth of 1D core-crystalline micelles upon annealing in solution. Macromolecules. 2016;49:7004–515.
72. Prasad I, Jinnai H, Ho R.-M, Thomas EL, Grason GM. Anatomy of triply-periodic network assemblies: characterizing skeletal and inter-domain surface geometry of block copolymer gyroids. Soft Matter. 2018;14:3612–23.
73. Kawase N, Kato M, Nishioka H, Jinnai H. Transmission electron microtomography without the "missing wedge" for quantitative structural analysis. Ultramicroscopy. 2007;107:8–15.
74. Fung JC, et al. Toward fully automated high-resolution electron tomography. J Struct Biol. 1996;116:181–9.
75. Frank J. Principles of electron tomography. New York: Plenum Press; 1992. p. 1–16.
76. Jinnai H, et al. Direct measurement of interfacial curvature distributions in a bicontinuous block copolymer morphology. Phys Rev Lett. 2000;84:518–21.
77. Wang YC, Wakabayashi M, Hasegawa H, Takenaka M. 3D-TEM study on the novel bicontinuous microdomain structure. Soft Matter. 2017;13:8824–8.
78. Wang YC, Inoue A, Hasegawa H, Takenaka M. The formation of otdd network structure in ps-*b*-pi-*b*-pdms triblock terpolymer. Macromol Chem Phys. 2017;218:1700008.
79. Lin, C.-H et al. Stabilizing the ordered bicontinuous double diamond structure of diblock copolymer by configurational regularity. Macromolecules. 2018;51:4049–58
80. Watson JD, Crick FH. Molecular structure of nucleic acids: a structure for deoxyribose nucleic acid. Nature. 1953;171:737.
81. Krappe U, Stadler R, Voigt-Martin I. Chiral assembly in amorphous abc triblock copolymers. formation of a helical morphology in polystyrene-*block*-polybutadiene-*block*-poly(methyl methacrylate) block copolymers. Macromolecules. 1995;28:4558.
82. Cornelissen J, Fischer M, Sommerdijk N, Nolte RJ. Helical superstructures from charged poly(styrene)-poly(isocyanodipeptide) block copolymers. Science. 1998;280:1427.
83. Ho R-M, et al. Three-dimensionally packed nanohelical phase in chiral block copolymers. J Am Chem Soc. 2004;126:2704.
84. Kloninger C, Rehahn M. Styrene-ferrocenyldimethylsilane-methyl methacrylate triblock copolymers: synthesis and phase morphology. Macromol Chem Phys. 2007;208:833.
85. Zhong S, Cui H, Chen Z, Wooley KL, Pochan DJ. Helix self-assembly through the coiling of cylindrical micelles. Soft Matter. 2008;4:647.
86. Tseng E-H, et al. Helical nanocomposites from chiral block copolymer templates. J Am Chem Soc. 2009;50:1067.
87. Wang Y, et al. Nanoscopic morphologies in block copolymer nanorods as templates for atomic-layer deposition of semiconductors. Adv Mater. 2009;21:1–4.
88. Dupont J, Liu G, Niihara K, Kimoto R, Jinnai H. Self-assembled ABC triblock copolymer double and triple helices. Angew Chem Int Ed. 2009;48:6144–47.
89. Higuchi T, et al. Morphological control of helical structures of an ABC-type triblock terpolymer by distribution control of a blending homopolymer in a block copolymer microdomain. Macromolecules. 2013;46:6991–7.
90. Yao L, Lu X, Chen S, Watkins JJ. Formation of helical phases in achiral block copolymers by simple addition of small chiral additives. Macromolecules. 2014;47:6547–53.
91. Wen T, Ho R.-M. Effects of the chiral interface and orientation-dependent segmental interactions on twisting of self-assembled block copolymers. ACS Macro Lett. 2017;6:370–4.
92. Nishikawa Y, Kawada H, Hasegawa H, Hashimoto T. Grain boundary morphology of lamellar microdomains. Acta Polym. 1993;44:247–55.
93. Gido SP, Gunther J, Thomas EL, Hoffman D. Lamellar diblock copolymer grain boundary morphology. 1. Twist boundary characterization. Macromolecules. 1993;26:4506–20.
94. Gido SP, Thomas EL. Lamellar diblock copolymer grain boundary morphology. 2. Scherk twist boundary energy calculations. Macromolecules. 1994;27:849–61.
95. Ehlich D, Takenaka M, Okamoto S, Hashimoto T. FRS study of the diffusion of a block copolymer. 1. Direct determination of the anisotropic diffusion of block copolymer chains in a lamellar microdomain. Macromolecules. 1993;26:189–97.
96. Ehlich D, Takenaka M, Hashimoto T. Forced Rayleigh scattering study of diffusion of block copolymers. 2. Self-diffusion of block copolymer chains in lamellar microdomains and disordered melts. Macromolecules. 1993;26:492–8.
97. Hadziioannou G, et al. Low-angle neutron scattering study of the lateral extension of chains in lamellar styrene isoprene block copolymers. Macromolecules. 1982;15:263–71.
98. Bates FS, Berney CV, Cohen RD, Wignall GD. Single-chain scattering in heterogeneous block copolymers. Polymer (Guildf). 1983;24:519–24.
99. Hasegawa H, et al. Sans and saxs studies on molecular conformation of a block polymer in microdomain space. Macromolecules. 1985;18:67–78.
100. Hasegawa H, Tanaka H, Hashimoto T, Han CC. SANS and SAXS studies on molecular conformation of a block polymer in microdomain space. 2. Contrast matching technique. Macromolecules. 1987;20:2120–7.
101. Matsushita Y, Torikai N, Mogi Y, Noda I, Han CC. Chain conformations of homopolymers dissolved in a microdomain of diblock copolymer. Macromolecules. 1994;27:4566–9.
102. Yang J, Sekine R, Aoki H, Ito S. Localization and orientation of homopolymer in block copolymer lamella: a near-field optical microscopy study. Macromolecules. 2007;40:7573–80.
103. Mayes AM, Russell TP, Satija SK, Majkrzak CF. Homopolymer distribution in ordered block copolymers. Macromolecules. 1992;25:6523–31.
104. Tamai Y, Sekine R, Aoki H, Ito S. Conformation of single homopolymer chain in microphase-separated block copolymer monolayer studied by scanning near-field optical microscopy. Macromolecules. 2009;42:4224–9.
105. Sekine R, Aoki H, Ito S. Conformation of single block copolymer chain in two-dimensional microphase-separated structure studied by scanning near-field optical microscopy. J Phys Chem B. 2009;113:7095–100.
106. Kremer K, Grest GS. Dynamics of entangled linear polymer melts: a molecular-dynamics simulation. J Chem Phys. 1990;92:5057–86.
107. Aoyagi T, Honda T, Doi M. Microstructural study of mechanical properties of the ABA triblock copolymer using self-consistent field and molecular dynamics. J Chem Phys. 2002;117:8153–61.
108. Torikai N, et al. Neutron reflection studies on segment distribution of block chains in lamellar microphase-separated structure. Macromolecules. 1997;30:2907–14.
109. Helfand E, Wasserman ZR. Block copolymer theory. 4. Narrow interphase approximation. Macromolecules. 1976;9:879–88.
110. Hong KM, Noolandi J. Theory of inhomogeneous multicomponent polymer systems. Macromolecules. 1981;14:727–36.
111. Matsen MW, Schick M. Stable and unstable phases of a diblock copolymer melt. Phys Rev Lett. 1994;72:2660–3.
112. Grest GS, Kremer K. Molecular dynamics simulation for polymers in the presence of a heat bath. Phys Rev A. 1986;33:3628–31.
113. Morita H, Kawakatsu T, Doi M, Nishi T, Jinnai H. Three-dimensional visualization of a single block copolymer in lamellar nanodomains. Macromolecules. 2008;41:4845–9.

114. Kawasaki K, Kawakatsu T. Equilibrium morphology of block copolymer melts. 3. Macromolecules. 1990;23:4006–19.
115. Zhao J, et al. Phase behavior of pure diblocks and binary diblock blends of poly(ethylene)-poly(ethylethylene). Macromolecules. 1996;29:1204–15.
116. Vigild ME, et al. Transformations to and from the gyroid phase in a diblock copolymer. Macromolecules. 1998;31:5702–16.
117. Kimishima K, Koga T, Hashimoto T. Order–order phase transition between spherical and cylindrical microdomain structures of block copolymer. i. Mechanism of the transition. Macromolecules. 2000;33:968–77.
118. Sugimori H, Niihara K, Kaneko T, Miyoshi W, Jinnai H. Direct three-dimensional observations of order–order transition from gyroid to cylindrical structures in a block copolymer. Progr Theor Phys Suppl. 2008;175:166–73.
119. Jung J, et al. Epitaxial phase transition between double gyroid and cylinder phase in diblock copolymer thin film. Macromolecules. 2014;47:8761–7.
120. Mareau VH, Akasaka S, Osaka T, Hasegawa H. Direct visualization of the perforated layer/gyroid grain boundary in a polystyrene-*block*-polyisoprene blend by electron tomography. Macromolecules. 2007;40:9032–9.
121. Dohi H, et al. Three-dimensional imaging in polymer science: Its application to block copolymer morphologies and rubber composites. Polym J. 2007;39:749–58.
122. Migunov V, et al. Rapid low dose electron tomography using a direct electron detection camera. Sci Rep. 2016;5:14516.
123. Kato K. Electron microscopy of ABS plastics. J Electron Microsc. 1965;14:220–1.
124. Aso R, et al. Quantitative imaging of T-g in block copolymers by low-angle annular dark-field scanning transmission electron microscopy. Macromolecules. 2013;46:8589–95.
125. Danev R, Nagayama K. Transmission electron microscopy with Zernike phase plate. Ultramicroscopy. 2001;88:243–52.
126. Jinnai H, et al. Three-dimensional visualization and characterization of polymeric self-assemblies by transmission electron microtomography. Acc Chem Res. 2017;50:1293–302.
127. Crowther RA, DeRosier DJ, Klug A. The reconstruction of a three-dimensional structure from projections and its application to electron microscopy. Proc R Soc Lond Ser A. 1970;317:319–40.
128. Zhuge X, Palenstijn W, Batenburg K. TVR-DART: a more robust algorithm for discrete tomography from limited projection data with automated gray value estimation. IEEE Trans Image Process. 2015;25:455–68.
129. Zhuge X, et al. Automated discrete electron tomography—towards routine high-fidelity reconstruction of nanomaterials. Ultramicroscopy. 2017;175:87–96.

Professor Hiroshi Jinnai is a Professor of the Institute of Multidisciplinary Research for Advanced Materials (IMRAM), Tohoku University. He received his D. Eng. in 1993 from Kyoto University, Japan. During his thesis study, he visited the National Institute of Standards and Technology (NIST), USA as a guest scientist. In 1993, he joined the Japan Science and Technology Agency (JST) ERATO (Exploratory Research for Advanced Technology) program, Hashimoto Polymer Phasing Project, as a group leader. He was appointed Lecturer at the Department of Macromolecular Science and Engineering of Kyoto Institute of Technology in 1998 and was promoted to Associate Professor in 2002. In 2011, He moved to another ERATO program, Takahara Soft Interfaces Project, as a research manager. He was concurrently a Research Professor at the Institute of Materials Chemistry and Engineering (IMCE), Kyushu University. Since 2015, he moved to Tohoku University. His research field includes soft matter physics and development of characterization methodology. Specifically, he is widely recognized by his development of electron tomography (3D electron microscopy). He was awarded the SPSJ (The Society of Polymer Science, Japan) Wiley Award in 2006. He is the first Japanese to win the biannual Ernst-Ruska-Prize in 2007 from the Deutsche Gesellschaft fur Elektronenmikroskopie (German Society of Electron Microscopy). He is also the recipient of The Japanese Society of Microscopy Society Award, Setoh Prize (2012), The Award of the Society of Polymer Science, Japan (2017), and so on. He is the Fellow of American Physical Society (APS).